

Spacecraft charging and ion wake formation in the near-Sun environment

R. E. Ergun,¹ D. M. Malaspina,¹ S. D. Bale,² J. P. McFadden,² D. E. Larson,²
F. S. Mozer,² N. Meyer-Vernet,³ M. Maksimovic,³ P. J. Kellogg,⁴ and J. R. Wygant⁴

¹The Laboratory for Atmospheric and Space Physics, University of Colorado, Boulder, Colorado 80309, USA

²Space Science Laboratory, University of California, Berkeley, California 94720, USA

³LESIA, Observatoire de Paris, CNRS, UPMC, Université Paris Diderot,

⁵Place Jules Janssen, 92195 Meudon, France

⁴Department of Physics and Astronomy, University of Minnesota, Minneapolis, Minnesota 55455, USA

(Received 5 April 2010; accepted 25 May 2010; published online 19 July 2010)

A three-dimensional, self-consistent code is employed to solve for the static potential structure surrounding a spacecraft in a high photoelectron environment. The numerical solutions show that, under certain conditions, a spacecraft can take on a negative potential in spite of strong photoelectron currents. The negative potential is due to an electrostatic barrier near the surface of the spacecraft that can reflect a large fraction of the photoelectron flux back to the spacecraft. This electrostatic barrier forms if (1) the photoelectron density at the surface of the spacecraft greatly exceeds the ambient plasma density, (2) the spacecraft size is significantly larger than local Debye length of the photoelectrons, and (3) the thermal electron energy is much larger than the characteristic energy of the escaping photoelectrons. All of these conditions are present near the Sun. The numerical solutions also show that the spacecraft's negative potential can be amplified by an ion wake. The negative potential of the ion wake prevents secondary electrons from escaping the part of spacecraft in contact with the wake. These findings may be important for future spacecraft missions that go nearer to the Sun, such as Solar Orbiter and Solar Probe Plus. © 2010 American Institute of Physics. [doi:10.1063/1.3457484]

I. INTRODUCTION

Spacecraft (SC) charging and wake formation have been a concern since the launch of the first orbiters. This concern arises for a variety of reasons including the safety of astronauts and the safeguarding of SC electrical systems.^{1,2} An understanding of and, in many cases, the control of SC charging also can be essential for *in situ* measurements of charged particles and electric fields.^{3–7} For these reasons, the charging of a body immersed in a plasma has been studied over the past several decades.^{1–15} We investigate SC charging and wake formation under strong photoelectron fluxes. The primary motivation of this study is that NASA (Ref. 16) and the European Space Agency¹⁷ are actively pursuing *in situ* plasma measurements near the Sun.

The nominal solar wind conditions at 1 astronomical unit (AU) are such that, if a SC were at zero potential ($\Phi_{SC}=0$), the sum of photoelectron current (I_{ph}), ion current (I_i), and secondary electron current (I_{se}) would exceed the thermal electron current (I_{the}) to a SC.^{1,4} Thus, a SC typically settles to a small positive potential of a few volts, reducing photoelectron and secondary electron currents so that the net current to the SC is zero.

With a small positive potential, the solar wind electron fluxes can be measured at all energies, although SC potential corrections are needed for deriving the distribution function, density, and velocity.^{6–9,18} Since the solar wind speed is almost always supersonic, the ion fluxes have high velocities with respect to the SC, so the most meaningful part of the ion distribution can be measured as well.^{6–9,18} As it turns out, the positive potential on SC in the solar wind is fortunate since a negative SC could hamper the measurement of core

electrons. Electric field measurements are somewhat more difficult in the solar wind since a negative potential well can form in the ion wake.^{3,4,8–10} Care must be taken in design of these instruments and subsequent data analysis.

Nearer to the Sun than 1 AU, the plasma environment changes considerably. However, the most significant currents between the ambient plasma and a SC scale roughly as $\sim 1/R^2$, where R is the distance from the Sun. If all parameters were to scale as $1/R^2$, a SC nearer to the Sun would be expected have, under most conditions, a positive potential as well. But, there are some parameters between 1 AU and the near-Sun environment that do not scale as $1/R^2$. The plasma Debye length scales roughly as R and electron and ion temperatures increase nearer to the Sun, so the potential in an ion wake is larger, whereas the characteristic energy of the photoelectrons and secondary electrons remain the same. These “higher-order” effects may cause the SC potential to deviate from the relatively benign potential of a few volts positive.

Analytical and numerical solutions of the charging and the plasma environment of the HELIOS SC (Refs. 8 and 9) highlighted some of the differences in SC charging nearer to the Sun. The numerical solutions show a deeper wake potential and significant electrostatic barriers produced by the SC photoelectrons. The studies were verified by examining the electron fluxes measured on the HELIOS SC.

We investigate SC charging and wake formation in the near-Sun environment with a three-dimensional (3D), self-consistent code. The code combines a Poisson solver and a particle tracing routine. We find that the ion wake has a negative potential that is a significant fraction of the thermal electron temperature (kT_e). This finding verifies previous

studies^{3,8–10} and punctuates that the wake effect near to the Sun is more significant than at 1 AU. The ion and electron temperatures are higher and, because the plasma density is much higher, the wake size is many Debye lengths. Another important finding is that the SC settles to a negative potential sometimes in excess of $-kT_e$, as low as ~ -100 V, in spite of the high photoelectron currents. (Since there are uncertainties in secondary electron production, the floating potential of a SC cannot be predicted with high accuracy.) These findings may impact both electric field^{3–5} and electron^{6–9} measurements on future missions.^{16,17}

Further analysis shows that the negative SC potential is primarily due to an electrostatic barrier^{1,8,9,11,19} which forms on the Sun-exposed surfaces of the SC. The electrostatic barrier comes from a combination of conditions, which include a small Debye length of the photoelectrons (λ_{ph}) and the high thermal electron temperatures. Essentially, the thermal electrons can penetrate the electrostatic barrier whereas photoelectrons and secondary electrons cannot. Furthermore, the negative potential of the ion wake prevents photoelectron fluxes and secondary electron fluxes from escaping the surfaces of the SC that contact the ion wake.^{19–21}

II. SC CHARGING OVERVIEW

For a conductive SC, charging is generally solved through balancing of the currents to and from the SC (Refs. 1 and 22)

$$I_{ph}(\Phi_{SC}) + I_I(\Phi_{SC}) + I_{se}(\Phi_{SC}) + I_{the}(\Phi_{SC}) + I_{other} = 0, \quad (1)$$

where I_{other} acknowledges that there may be currents not considered here, for example, thermionic currents. For this work, we set $I_{other} = 0$. Each of these currents varies with the SC potential (Φ_{SC}). The roots of the above equation yield Φ_{SC} . Generally, there is only one root to this equation but multiple roots are possible if the electron distribution is non-Maxwellian and the electron secondary yield is high,^{1,23} or if nonmonotonic potentials surround the SC.²⁴ If the SC is nonconducting or has electrically isolated surfaces, each surface must be solved separately.

I_{ph} depends on the projected area of the SC that is exposed to sunlight convolved with the photoelectron yield (J_{ph0}), which, in turn, depends on the intensity of the sunlight and the properties of the material. For most SC conducting materials, J_{ph0} ranges from ~ 20 to ~ 60 $\mu\text{A}/\text{m}^2$ at 1 AU.^{1,4,5} Often, the photoelectron yield increases after long exposure to space vacuum over that measured in the laboratory.^{4,13} We will use 20 $\mu\text{A}/\text{m}^2$ as a low yield and 57 $\mu\text{A}/\text{m}^2$ as a high yield⁴ at 1 AU. The photoelectron spectrum yields a current that varies with the SC potential. This relation has been previously described as a double exponential⁴

$$J_{ph} = J_{ph0}[(1 - \alpha)e^{-\Phi_{SC}/V_1} + \alpha e^{-\Phi_{SC}/V_2}], \quad \Phi_{SC} \geq 0, \quad (2)$$

where $V_1 = 2.7$ V, $V_2 = 10$ V, and $\alpha = 5\%$. $J_{ph} = J_{ph0}$ if $\Phi_{SC} < 0$.

In the solar wind environment, I_I is insensitive to the SC potential in all but the most extreme cases. The solar wind velocity, ~ 300 km/s, is such that ions can penetrate a barrier as high as ~ 1 kV. I_I is determined from the product of

the projected area of solar wind impact, the solar wind speed, and the solar wind density. Since little is known about the absorption efficiency, we assume it to be 100%. We show later that Φ_{SC} is only moderately sensitive to the ion absorption efficiency.

To lowest order, thermal electron current is related to the thermal flux of electrons impinging on a SC

$$J_{the0} = en\sqrt{kT_e/(2\pi m_e)}, \quad (3)$$

where e is the fundamental charge, n is the plasma density, k is Boltzmann's constant, and m_e is the electron mass. The thermal electron current is incident to the entire exposed area of the SC. If the SC is positively charged, the electron current can increase due to focusing²²

$$J_{the} = J_{the0}(1 + \Phi_{SC}/kT_e), \quad 0 \leq \Phi_{SC} \ll kT_e. \quad (4)$$

Equation (4) is an approximation for a sphere with a radius smaller than the Debye length. Otherwise the thermal electron current decreases

$$J_{the} = J_{the0}e^{\Phi_{SC}/kT_e}, \quad \Phi_{SC} < 0. \quad (5)$$

For most materials, the absorption efficiency is nearly 100% for low-energy (< 50 eV) electrons,¹ but can decrease above few hundred eV.

I_{se} , while important,^{20,21} is difficult to predict. The emission of secondary electrons comes from both ion impact and electron impact. The efficiencies depend on the energy of the impacting particle and are not well established for many materials. In the solar wind, the ion impact efficiencies are expected to be close to 100%, in effect making the secondary electron current from ion impact nearly equal to I_I . To derive the contribution of I_{se} from electron impact, one must convolve the electron fluxes with the secondary yield as a function of energy. The secondary yield is near zero for low-energy electrons (< 10 eV) but can be greater than unity if the electron energies are ~ 100 eV, so the net efficiency of the electron secondary emission can vary between near zero to greater than 100%.²³ The spectrum of secondary electrons typically has a characteristic energy, $V_{se} \sim 2$ eV.¹ Thus the electron secondary currents vary with Φ_{SC} as

$$J_{se} = J_{se0}(\Phi_{SC})e^{-\Phi_{SC}/V_{se}}, \quad \Phi_{SC} \geq 0. \quad (6)$$

Analytic solutions to Eq. (1) are often not possible, but simple approximations can be made. For example, in the 1 AU solar wind environment, $kT_e > V_1$ and the photoelectron current is larger than all other currents. One can set $I_{the} = I_{the0}$ and assume I_I and I_{se} are small

$$\Phi_{SC} \equiv V_1 \ln(-I_{ph}/I_{the}), \quad (7)$$

where, by convention, I_{the} is negative and I_{ph0} is positive (current to SC is positive). This approximation yields a few volts positive potential in the solar wind. In many plasma environments, this approximation is useful but is not necessarily accurate, particularly if the SC geometry is not spherical.²⁵

A solution to Eq. (1) would have the underlying assumption that the paths of the charged particles to the SC are not altered by the surrounding potential as to change the net current, except as allowed in Eqs. (2)–(6). Closer to the Sun,

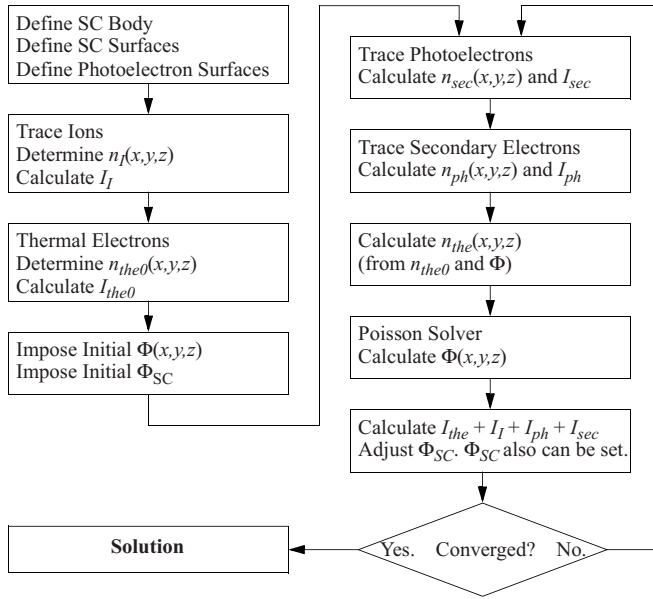


FIG. 1. The basic architecture of the Poisson/electron tracing code.

however, the charge density of photoelectrons is sufficient to develop nonmonotonic potentials which may significantly change the currents to the SC. We investigate this behavior with a numerical code.

III. DESCRIPTION OF NUMERICAL CODE

A fully 3D and a 3D cylindrically symmetric Poisson solver and electron tracing programs are employed to examine the potential structure surrounding a SC. The primary motivation is to determine the error sources in the electric field and electron measurements from the ion wake and non-monotonic potential structures from intense photoelectron currents. The code is a substantially modified version an earlier code used for the Cluster SC.²⁶ It includes the ion wake, Debye shielding, and secondary electron emission as well as photoelectrons.

For the fully 3D solutions, a model of a SC is placed in the center of a $20 \times 20 \times 20 \text{ m}^3$ box on a $200 \times 200 \times 200$ cubic grid with 10 cm spacing. Another version of the code has 3D, cylindrically symmetric domain on a two-dimensional (2D) grid. It allows for finer grid spacing and has significantly faster convergence. The domain is a 5 m (in r) \times 10 m (in x) cylinder with 250×500 2D grid. The grid spacing is 2 cm in both x and r . Particle tracing is in 3D. Both codes have two parts, which (1) determine the potential structure (Φ) surrounding the SC via a Poisson solver (given a charge distribution) and (2) determine the charge distribution via particle tracing (given Φ). The two parts of the code are iterated until they converge to a self-consistent solution. Figure 1 shows the basic algorithm.

We treat the SC as conducting. We can allow for some nonconduction areas by setting them at a fixed potential, for example, the front side of the solar arrays in the Solar Probe Plus SC are assumed to be nonconducting.¹⁶ Since the fully

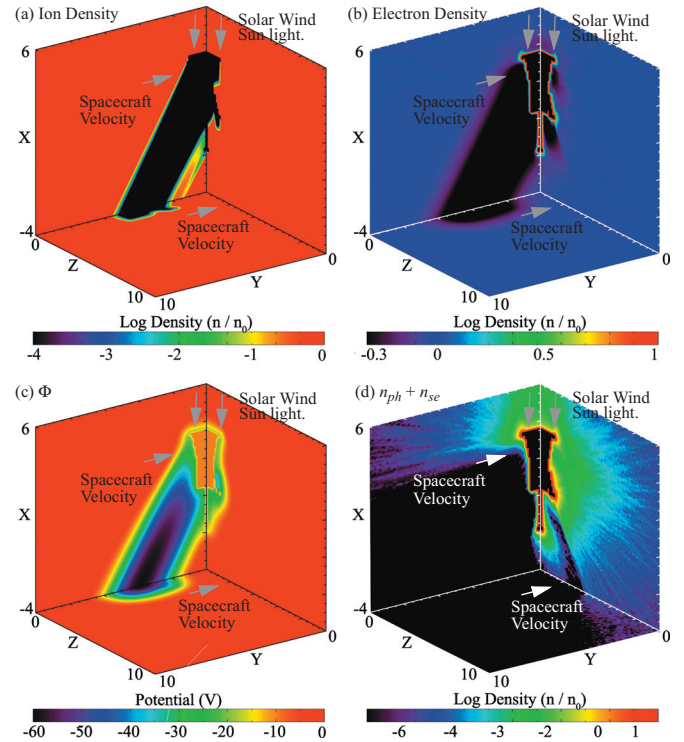


FIG. 2. (Color) (a) A 3D rendering of the ion density surrounding a model of the Solar Probe Plus SC at $9.5 R_S$. x is toward the Sun, z is normal to the ecliptic plane, and y completes the triad. The distances are in meters. The solar wind speed is 300 km/s in the $-x$ direction and SC is traveling at 180 km/s in the $-y$ direction. The plasma density is 7000 cm^{-3} and the ion temperature is set at 82 eV. (b) The electron density: $n_e = n_{ph} + n_{se} + n_{the}$. The thermal electrons ($T_e = 85 \text{ eV}$) dominate except for a thin layer surrounding the SC. (c) The self-consistent potential (Φ). Φ_{SC} is $\sim -10 \text{ V}$. The potential well in the bottom left is created by the ion wake. A thin layer of negative potential is surrounding the SC; it is particularly strong on the sunward side of the SC. (d) The photoelectron and secondary electron densities. All but $\sim 1\%$ of the photoelectrons are reflected back to the SC. The ion wake prevents secondary electrons from escaping from the left side.

3D SC is constructed of 10 cm cubes, fine detail cannot be included. A thin appendage has a minimum dimension of 10 cm.

The ion density is determined by streaming $\sim 10^8$ ions through the box, deriving the density from the integrated dwell time inside of the grid cubes. The dominant ion motion is from the solar wind velocity ($\sim 300 \text{ km/s}$) and the SC ram. For example, the Solar Probe Plus SC could have a velocity up to 180 km/s perpendicular to the solar wind near perihelion. The ions are initiated with the solar wind and ram speed, plus a random velocity that emulates a temperature (T_i), which ranges from a few eV at 1 AU to nearly 100 eV at $10 R_S$ (solar radii) from the Sun. Ions that strike the SC are removed, creating a wake in the antiram side of the SC. This derived ion density is held fixed when deriving the solutions (Φ). One can verify *a posteriori* that ion current to the SC and the ion density surrounding the SC are not sensitive to the potential structure (Φ) surrounding the SC.

The baseline thermal electron density (n_{the0}) is derived in a similar fashion, except that the electrons impinge on the SC from all sides, creating a modest electron well surrounding the SC. The resulting electron density is smoothed to remove

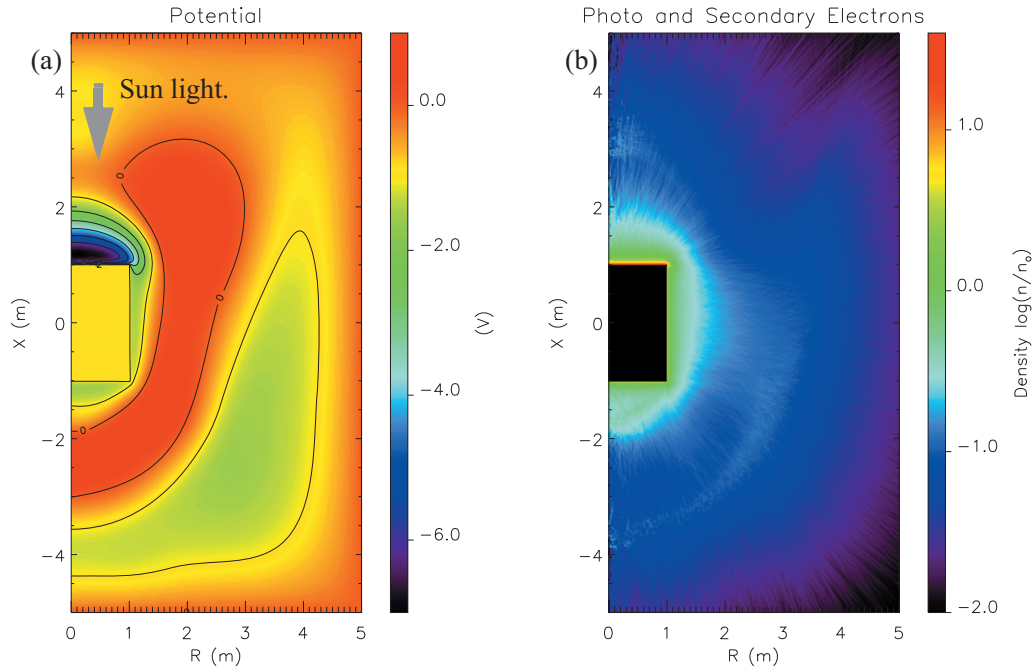


FIG. 3. (Color) A 3D, cylindrically symmetric solution of a cylindrically shaped SC at $9.5 R_S$. The photoemission and electron distribution mimic the solar wind at $9.5 R_S$, but the ion density is fixed. (a) Φ surrounding the SC. Φ_{SC} is -0.85 V. A negative potential envelops the surface of the SC and a barrier is formed at $x=+1.15$ m. The $\sim +1$ V structure ~ 1 m from the SC comes from a loss of thermal electron density due to partial physical shielding by the SC. (b) The photoelectron and secondary electron densities. A thin layer of high electron density surrounds the SC.

noise. Once Φ is determined, the thermal electron density is treated as a Boltzmann fluid

$$n_{\text{the}} = n_{\text{the0}} e^{\Phi/kT_e}. \quad (8)$$

This treatment allows for self-consistent Debye shielding and is valid as long as Φ is negative or, if positive, $\Phi \ll T_e$.

The code then derives the photoelectron density by tracing photoelectrons emitted from the sunlit surfaces in the surrounding potential structure.²⁶ Photoelectrons ($\sim 10^6$ particles in all) are randomly created on the sunlit surfaces with isotropic directions and an energy profile of a double exponential with characteristic energies of 2.7 and 10 eV [Eq. (2)] using a root emission of $57 \mu\text{A}/\text{m}^2$ at 1 AU, scaled to the location of the SC. In some cases, a root emission of $20 \mu\text{A}/\text{m}^2$ is also used for comparison with the higher emission results. Individual particles are traced by a “leap-frog” scheme in which the position is advanced then the velocity is advanced. The density is determined from the accumulated dwell time of particles within each of the grid cubes. The tracing continues until the particles either strike the SC or exit the code’s boundaries. Those that exit the code’s boundaries are considered lost and counted in the overall photoelectron current from the plasma to the SC. The secondary electron density is derived in a similar fashion, randomly creating secondary electrons over the SC surface with 2 eV characteristic energy and an overall production efficiency ε_{sec} estimated by convolving the electron flux energy profile with a published efficiency profile for BeCu.^{1,23} Again, we emphasize that the secondary electron production has significant uncertainty.

The SC potential is estimated by balancing the currents. Once the ion, thermal electron, photoelectron, and secondary

electron densities are established, the potential is derived from a Poisson solver over the entire grid, holding the SC surfaces at constant potential and the boundaries at zero. The process of photoelectron tracing, secondary electron tracing, thermal electron density derivation, SC potential calculation, followed by a Poisson solver is repeated until a self-consistent solution converges (Fig. 1). The primary convergence criterion is the maximum change in Φ in the code’s domain ($\Delta\Phi_{\text{max}}$). Depending on how many particles are used, $\Delta\Phi_{\text{max}}$ ranges from 1 to 25 mV.

The Poisson solvers, both the fully 3D and 3D cylindrically symmetric versions, have a iterative convergence of

$$\nabla^2 \Phi = -\rho/\varepsilon_0 = -(\rho_{\text{ion}} - \rho_{\text{the}} - \rho_{\text{phe}} - \rho_{\text{se}})/\varepsilon_0, \quad (9)$$

where ρ_{ion} , ρ_{the} , ρ_{phe} , and ρ_{se} , are, respectively, the ion charge density, the thermal electron charge density, the photoelectron charge density, and the secondary electron charge density. In each iteration, the value of Φ is set to $\Phi_{\text{av}} + \rho \delta x^2 / 6\varepsilon_0$, where Φ_{av} is the average of Φ in the surrounding grids and δx is the grid spacing.

IV. RESULTS

Figure 2(a) displays a 3D rendering of the ion density and resulting wake (x is toward the Sun, z is normal to the ecliptic plane, and y completes the triad) from a model of the Solar Probe Plus SC at $9.5 R_S$ from the Sun. The solar wind speed is 300 km/s in the $-x$ direction and the SC speed is 180 km/s in the $-y$ direction. Figure 2(b) shows the electron density (all electron populations), Fig. 2(c) displays the self-consistent potential surrounding the SC and Fig. 2(d) displays the photoelectron and secondary electron densities

TABLE I. Currents to SC.

No wake (Figs. 3 and 4)	($\Phi_{SC}=0$) Current (mA)	Efficiency	Predicted current ($\Phi_{SC}=0$)	Numerical solution ($\Phi_{SC}=-0.85$ V)
I_{ph}	91.1	29 mA/m ²	91.1	7.4
I_{the}	-18.0	85%	-15.3	-15.2
I_I	1.4	100%	1.4	1.4
I_{se}	16.7	100%	16.7	6.4

as a fraction of the background density (n_0). The plots show cuts through three planes. The expected plasma conditions at $9.5 R_S$ are $n_0=7000$ cm⁻³, $T_e=85$ eV, and $T_i=82$ eV. The high-yield photoelectron current is used. Scaled to $9.5 R_S$, $J_{ph0}=29$ mA/m². The average electron absorption efficiency is set at 85% (estimated from T_e), the ion absorption efficiency is set at 100%, and the electron secondary production efficiency is estimated at 100% for both ion and electron impacts.

The potential in the center of the wake is below -60 V [Fig. 2(c)] due to the ion vacuum [Fig. 2(a)]. The deep ion wake potential is expected since the scale size of the wake, $\sim 2-3$ m in diameter, is larger than the thermal electron Debye length ($\lambda_D=0.76$ m). The center of the wake is expected to see potentials on the order of T_e . The temperature of the thermal electrons is such that they easily penetrate the electrostatic barrier surrounding the SC, but are significantly altered in the ion wake region [Fig. 2(b)]. They also have a significant shielding effect. The plasma potential ~ 5 m from the SC is nearly zero.

Figure 2(c) also shows a thin layer of negative potential surrounding the SC. It is particularly strong on the sunward side of the SC due to the high photoelectron density ($>10^6$ cm⁻³), also in a thin layer [Figs. 2(b) and 2(d)]. The nonmonotonic, electrostatic barrier prevents the low-energy part of photoelectrons and secondary electrons from escaping. On the top of the SC, the electrostatic barrier is ~ -8 V and reflects $\sim 99\%$ of the photoelectron current and $>99\%$ of the secondary electrons back to the SC. A smaller (<1 V) barrier is seen around the other SC surfaces. These barriers ultimately cause the SC to have negative potential: ~ -10 V.

Figure 2(d) also shows that secondary electrons do not escape from the areas of the SC that are contacting the ion wake. The secondary production is smaller since less thermal electrons reach the surface contacting the wake. More importantly, the negative wake potential (-60 V) very efficiently reflects these secondary electrons (~ 2 eV) back to the SC. This wake reflection amplifies the negative potential of the SC.

In the 3D solutions, the electrostatic barrier is mostly carried in one grid layer, so it is examined further with a series of 3D, cylindrically symmetric numerical solutions of a simple, fully conducting cylinder, 1 m in radius and 2 m long, with one end allowed to emit photoelectrons. This controlled experiment allows us to investigate the conditions that cause the negative charging.

Figure 3 shows a solution that has no ion wake. The ions

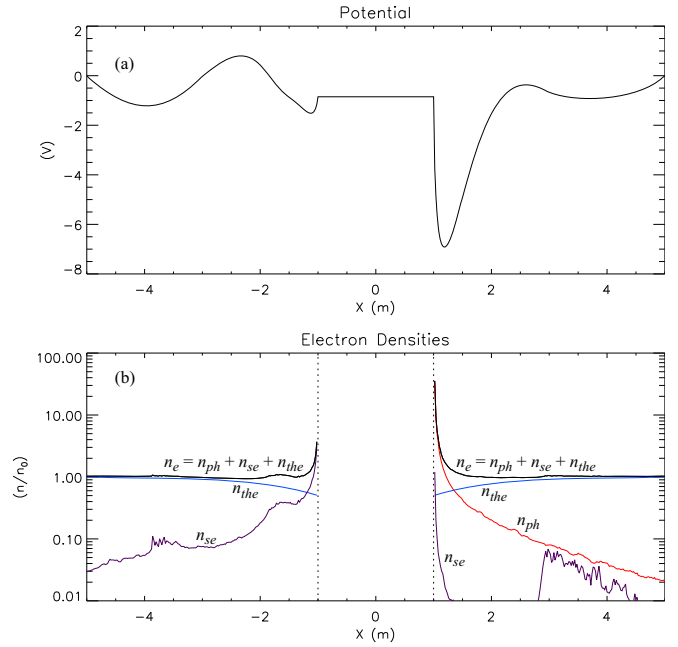


FIG. 4. (Color online) (a) A line plot of $\Phi(x)$ along the $r=0$ axis of the solution derived from Fig. 3(a). The potential of the SC is -0.85 V. A -6 V (with respect to Φ_{SC}) electrostatic barrier forms at $x=+1.15$ m. A smaller barrier is seen at $x=-1.15$ m. (b) The electron densities along the $r=0$ axis. The lines are labeled on the plot. The vertical dashed lines indicate the top and bottom surfaces of the SC.

are artificially held at a fixed density. This condition is unrealistic, but is useful to examine the effect of the ion wake. The plasma conditions are otherwise identical to those in Fig. 2 as are the electron absorption and electron secondary emission efficiencies. Figure 3(a) displays Φ and Fig. 3(b) displays the $n_{ph}+n_{se}$. Φ_{SC} is -0.85 V. The currents to the SC are in Table I. In Fig. 3(a), one can clearly see an electrostatic barrier on the top face of the cylinder, the face that has photoelectrons. A smaller electrostatic barrier also surrounds the SC on all sides. This negative barrier comes from the large n_{ph} (1.1×10^6 cm⁻³) and n_{se} (2.9×10^4 cm⁻³) that forms in a thin layer around the SC.

Figure 4(a) plots the potential along the $r=0$ axis of the solution. The electrostatic potential on the top of the SC ($x=1.15$ m) is -6.9 V causing a barrier of approximately -6.1 V with respect to Φ_{SC} . Effectively, this electrostatic barrier reflects 92% of the photoelectrons back to the SC (Table I). Figure 4(b) plots n_{ph} (red), n_{se} (purple), n_{the} (blue), and their sum $n_e = n_{ph} + n_{se} + n_{the}$ (black) along the same axis. The vertical dashed lines are the edges of the SC. The thin layer of high electron charge is seen at both ends of the SC. The charge layer at the $x=1$ m end, is primarily from SC photoelectrons. Using $n_{ph}=10^6$ cm⁻³ and $T_{ph}=3$ eV, the photoelectron Debye length is ~ 15 cm, the thickness of the electrostatic barrier. The location of the barrier, about a photoelectron Debye length from the SC, is roughly that predicted from analytic solutions of a flat plate.²⁴ The depth of the electrostatic barrier (~ -6 V) is such that the escaping photoelectrons are from the higher-energy tail [Eq. (2)].

Figure 4(a) also shows a mild electrostatic barrier on the $x=-1$ m side of the SC. The minimum potential at

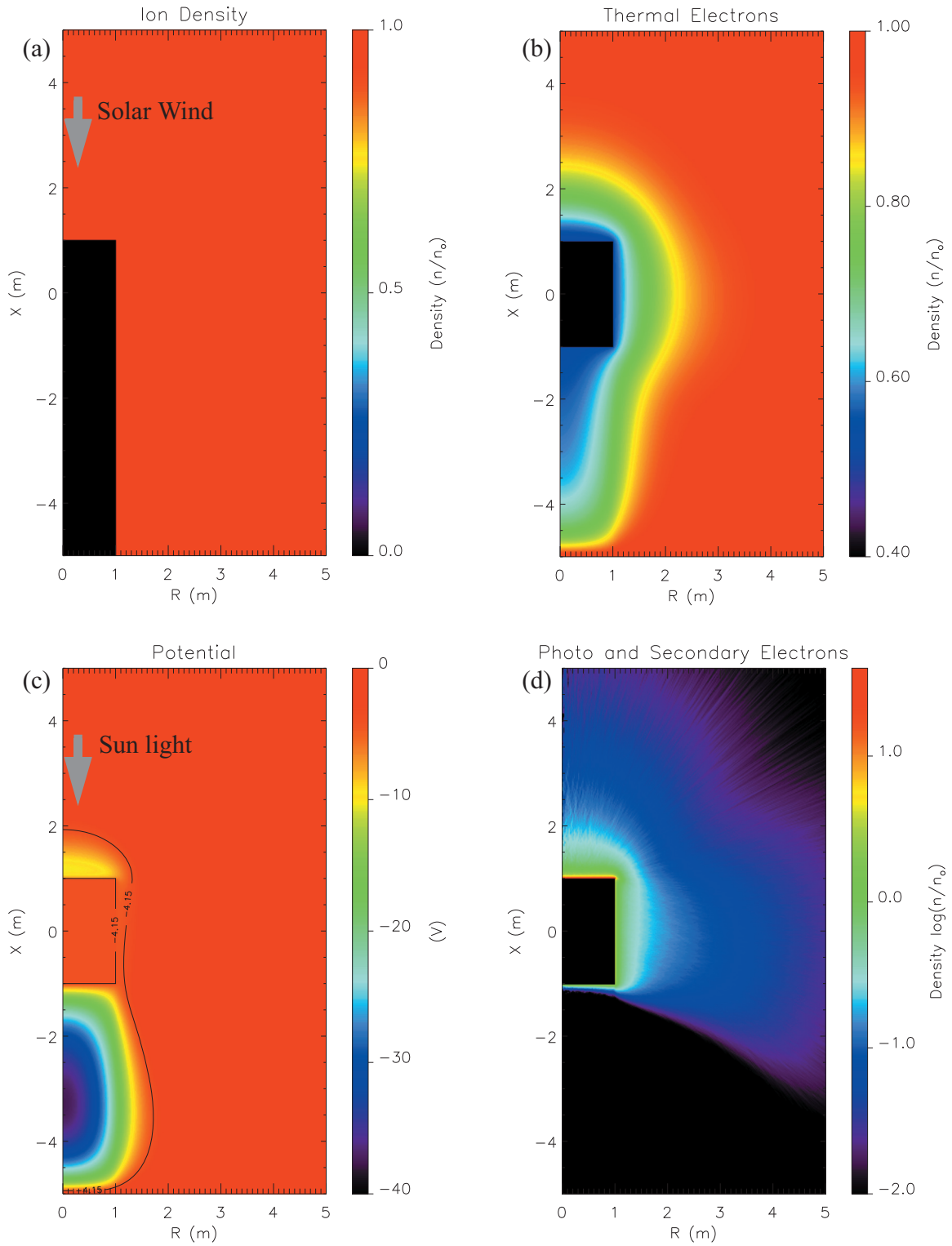


FIG. 5. (Color) (a) The ion density. A wake is on the $-x$ side of the SC. The ion temperature is zero. (b) The thermal electron density. (c) The self-consistent solution of Φ . (d) The photoelectron and secondary electron densities. Secondary electrons cannot escape from the bottom of the SC.

$x = -1.15$ m forms a barrier of ~ -0.3 V. This barrier, due to secondary electrons, causes approximately a 15% loss of secondary electron current. Figure 4(a) shows an overshoot of the potential at $x = -2.3$ m and $x = 2.5$ m. This overshoot is due to the shadowing of the thermal electrons by the SC whereas the ion density is fixed at n_0 . In the solar wind environment, a fixed ion density is realistic on the $+x$ side of

the SC, but one would expect an ion wake on the $-x$ side of the SC.

The same solution (as in Fig. 3) is repeated, this time with an ion wake. Figure 5(a) shows the ion density with an ion wake on the $-x$ side of the SC. The ion temperature is ignored, so the wake has a complete ion vacuum. Figure 5(b) displays the thermal electron density, Fig. 5(c) displays Φ ,

TABLE II. Currents to SC.

Ion wake (Fig. 5)	($\Phi_{SC}=0$) Current (mA)	Efficiency	Predicted current ($\Phi_{SC}=0$)	Numerical solution ($\Phi_{SC}=-4.15$ V)
I_{ph}	91.1	29 mA/m ²	91.1	7.8
I_{the}	-18.0	85%	-15.3	-14.6
I_I	1.4	100%	1.4	1.4
I_{se}	16.0	100%	16.0	5.4

and Fig. 5(d) displays $n_{ph} + n_{se}$. The SC potential is -4.15 V. Φ reaches -37 V in its center of the ion wake. The secondary electrons cannot escape from the $-x$ side of the SC [Fig. 5(d)], so the secondary electron current is decreased (Table II). Comparing the solutions in Figs. 3 and 5, one can see that the ion wake amplifies the negative charging of the SC. In this example, the areas of the SC from which secondary electrons cannot escape are the top and bottom ends, which are about 1/3 of the total area of the SC. The ion wake and the electrostatic barrier in the Solar Probe Plus solution (Fig. 2) block over one-half of the SC area, causing the Φ_{SC} to have a more negative value.

Figure 6 displays the results of a solution with conditions four times farther from the Sun, $n_0 = 440$ cm⁻³, $T_e = 25$ eV, and the photoelectron yield reduced by a factor of 16, to 1.8 mA/m². The same absorption and production efficiencies are used. Figure 6(a) displays Φ and Fig. 6(b) shows $n_{ph} + n_{se}$. In this case, $\Phi_{SC} = 2.9$ V. The electrostatic barrier at the top of the SC is much weaker. In particular, photoelectrons have a clear path radially outward. If $\Phi_{SC} = 0$, I_{ph} would greatly exceed I_{the} , so the SC charges to a positive potential as is often the case at 1 AU.

As a further test, a solution is found for a 1/4 scale model of the SC under the same plasma conditions as in Fig. 5. Figure 7 displays the results. The SC is 0.25 m in radius and 0.5 m long and the code's domain is also 1/4 in size, 1.25 m in r , and 2.5 m in x . The SC charges to a small, positive potential (0.3 V).

V. DISCUSSION AND CONCLUSIONS

The 1/4-scale model of SC floats to a positive potential in the same plasma conditions that the full-scale model has a negative potential. This conspicuous difference can be understood by comparing the scale size of the electrostatic barrier (λ_{Dph}) with the size of the SC (R_{SC}). If $R_{SC} \gg \lambda_{Dph}$, the photoelectron current essentially can be treated as an one-dimensional (1D) problem.²⁴ Near the center ($r=0$) of the top of the SC ($x=1$ m), $n_{ph} \gg n_{the}$, n_I , and n_{se} , causing a high negative charge layer, so Φ falls rapidly with distance (along x) from the SC. Therefore, n_{ph} falls rapidly

$$n_{ph}(x) = n_{ph0} e^{(\Phi(x) - \Phi_{SC})/kT_{ph}}, \quad (10)$$

where T_{ph} is a characteristic temperature of the photoelectrons. This decrease in Φ and n_{ph} can occur even if Φ_{SC} is negative. This effect is seen in Fig. 4.

$\Phi(x)$ continues to decrease with x until, $n_{ph} = n_I - n_{the}$, assuming n_{se} is negligible. Near the SC, n_{the} is less than n_I because the electron fluxes are partially physically screened by the SC whereas the ions fluxes are not screened except in the ion wake. In an 1D solution, the electrostatic barrier builds until $n_{ph} = \epsilon n_I$, where $\epsilon < 1$. Charge balance will occur at a distance from the SC of several λ_{Dph} . If $R_{SC} \leq \lambda_{Dph}$, the problem is treated in 2D or 3D, so n_{ph} will naturally fall with distance from the SC with or without the electrostatic barrier. For this reason, SC at 1 AU show a much milder barrier.¹¹

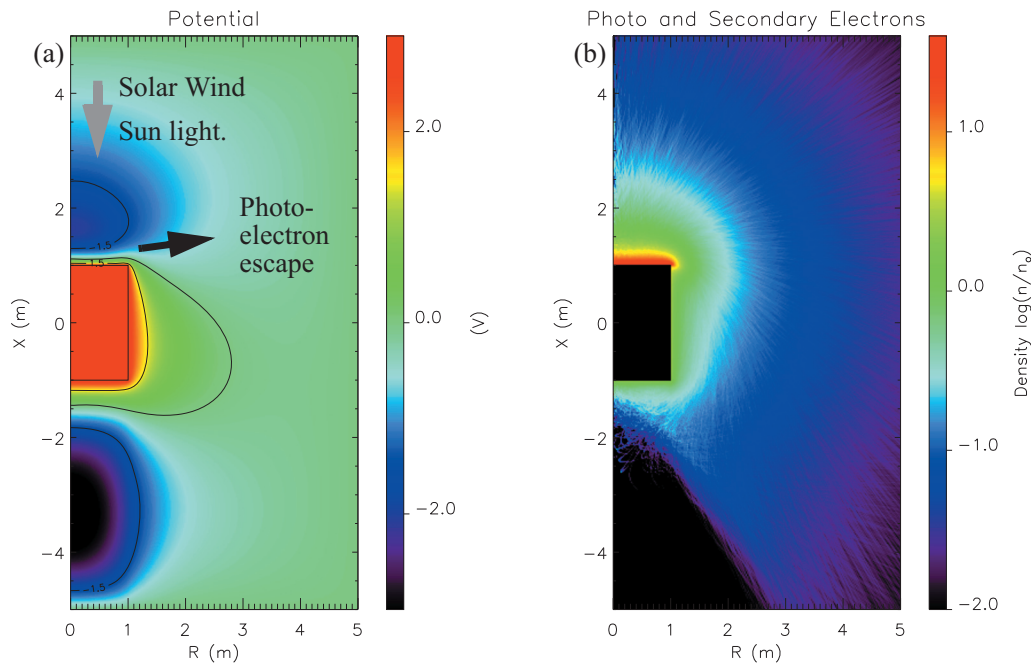


FIG. 6. (Color) The solution under conditions four times farther from the Sun. $n_0 = 440$ cm⁻³, $T_e = 25$ eV, and the photoelectron yield is reduced by a factor of 16, to 1.8 mA/m². (a) Φ . The SC is at 2.9 V. (b) The photoelectron and secondary electron densities.

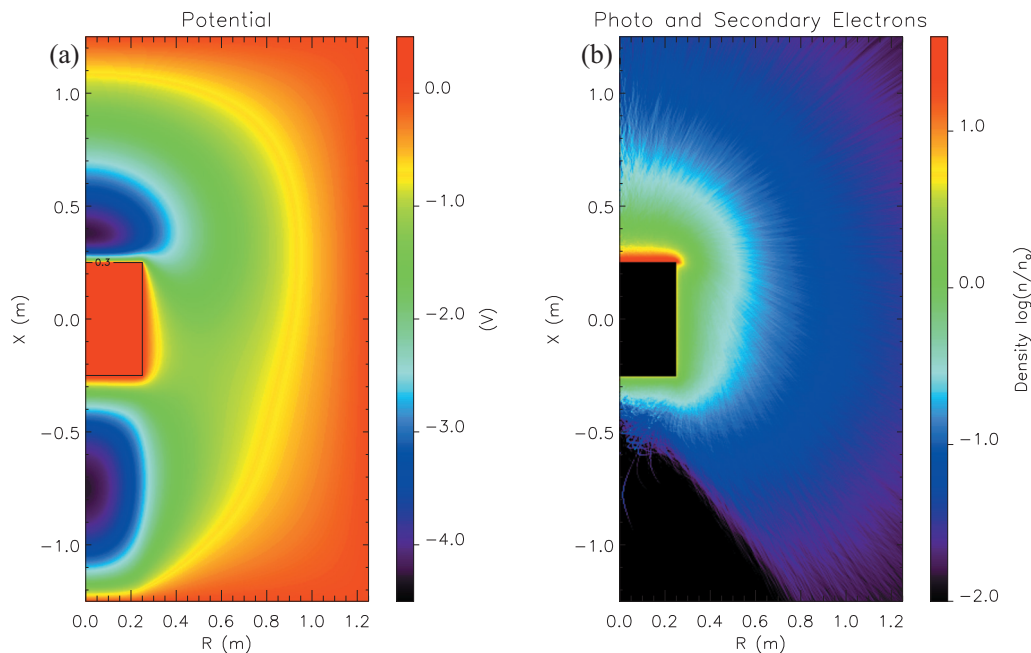


FIG. 7. (Color) The solution of a scaled model (1/4 size) with the same conditions as in Fig. 5. $n_0 = 7000 \text{ cm}^{-3}$, $T_e = 85 \text{ eV}$, and the photoelectron yield is 29 mA/m^2 . The SC is 0.25 m in radius and 0.5 m long. The solution's domain is 1/4 size as well. (a) Φ . The SC is at 0.3 V . (b) The photoelectron and secondary electron densities.

Ultimately, if n_{ph} is limited to a fraction of n_i , the limiting photoelectron current from the SC is $J_{phL} = \epsilon \epsilon n_i v_{ph}$, where v_{ph} is a characteristic velocity of the photoelectron flux at the limiting point. With a significant barrier, v_{ph} will be $\sim 10^6 \text{ m/s}$, the speed of a 10 eV electron due to the high-energy tail in the photoelectron fluxes. Since the thermal electron speed is larger, $J_{phL} \ll J_{the} = \epsilon n_i v_{the}$. We conclude that if (1) $R_{SC} \gg \lambda_{Dph}$ and (2) $v_{the} > \epsilon v_{ph}$, the thermal electron current will exceed the photoelectron current so the SC may charge to a negative potential. The solution in Fig. 5 has $R_{SC} = 1 \text{ m}$ and $\lambda_{Dph} \sim 0.15 \text{ m}$, whereas the solution in Figs. 6 and 7 have R_{SC} and λ_{Dph} nearly equal. The model of the Solar Probe Plus SC has $R_{SC} \gg \lambda_{Dph}$.

Interestingly, if $R_{SC} \gg \lambda_{Dph}$, the escaping photoelectron current does not strongly depend on the photoelectron yield at the surface of the SC (J_{ph0}), as long as it is sufficient to form an electrostatic barrier. The solution in Fig. 5 is only slightly different if the low-yield value of J_{ph0} is used.

The SC will not necessarily charge to a negative potential if I_{se} is comparable to I_{the} . However, the numerical solutions show that, even under high secondary yields (100%), the SC can charge to a negative potential because I_{se} is reduced by (1) the electrostatic barrier on the top of the SC caused by the photoelectrons, (2) a small barrier caused by the secondary electrons, and (3) the negative potential of the ion wake. These reductions cause the model of the Solar Probe Plus SC to float to $\sim -10 \text{ V}$ in our solutions. With lower secondary yield (50%), the negative charging becomes more severe and can be lower than $\Phi_{SC} \sim -kT_e$ (-85 V).

We examined the possibility of multiple roots^{1,23,24} in Eq. (1). Multiple roots are possible if the electron distribution is non-Maxwellian and the electron secondary yield is high,^{1,23} or if nonmonotonic potentials surround the SC.²⁴ We

used the same Poisson-based code to search for multiple roots from nonmonotonic potentials by fixing Φ_{SC} , forcing a solution, then recording the net current to the SC. (The distributions are modeled as Maxwellian, so multiple roots due to non-Maxwellian distributions could not be uncovered.) We could not find evidence for multiple roots. We, however, cannot rule out multiple roots since we examined only a small number of cases. The possibility of multiple roots is a subject for future research.

In conclusion, numerical solutions show that the SC can charge to a negative potential in spite of very high photoelectron fluxes. This behavior can be understood by comparing the size of the SC with the photoelectron Debye length. If $R_{SC} \gg \lambda_{Dph}$ and T_e is significantly larger than the characteristic energy of photoelectrons, an electrostatic barrier can form on the sunlit surfaces that reflects part of the photoelectron flux back to the SC. The negative SC potential is amplified by the fact that the secondary electron fluxes cannot penetrate the same electrostatic barrier and, if an ion wake forms, they cannot escape from the area of the SC that contacts the ion wake. Depending on the secondary electron yield, the Φ_{SC} can range from a few volts negative to as much as $\Phi_{SC} \sim -kT_e$ on a model of the Solar Probe Plus SC. This charging could compromise the measurement of the electron distribution and electric fields.

¹E. C. Whipple, *Rep. Prog. Phys.* **44**, 1197 (1981).

²H. B. Garrett, *Rev. Geophys. Space Phys.* **19**, 577, doi:10.1029/RG019i004p00577 (1981).

³A. I. Eriksson, M. André, B. Klecker, H. Laakso, P.-A. Lindqvist, F. Mozer, G. Paschmann, A. Pedersen, J. Quinn, R. Torbert, R. K. Torkar, and H. Vaith, *Ann. Geophys.* **24**, 275 (2006).

⁴A. Pedersen, *Ann. Geophys.* **13**, 118 (1995).

- ⁵A. Pedersen, B. Lybekk, M. André, A. Eriksson, A. Masson, F. S. Mozer, P.-A. Lindqvist, P. M. E. Décréau, I. Dandouras, J.-A. Sauvaud, A. Fazakerley, M. Taylor, G. Paschmann, K. R. Svenes, K. Torkar, and E. Whipple, *J. Geophys. Res.* **113**, A07S33, doi:10.1029/2007JA012636 (2008).
- ⁶V. Génot and S. J. Schwartz, *Ann. Geophys.* **22**, 2073 (2004).
- ⁷M. L. Adrian, *Phys. Plasmas* **9**, 602 (2002).
- ⁸U. Isensee, *J. Geophys.* **42**, 581 (1977).
- ⁹U. Isensee and H. Maassberg, *Adv. Space Res.* **1**, 413 (1981).
- ¹⁰E. Engwall, A. I. Eriksson, and J. Forest, *Phys. Plasmas* **13**, 062904 (2006).
- ¹¹B. Thiébaud, A. Hilgers, E. Sasot, H. Laakso, and P. Escoubet, *J. Geophys. Res.* **109**, A12207, doi:10.1029/2004JA010398 (2004).
- ¹²C. P. Escoubet, A. Pedersen, R. Schmidt, and P. A. Lindqvist, *J. Geophys. Res.* **102**, 17595, doi: 10.1029/97JA00290 (1997).
- ¹³R. Schmidt and A. Pedersen, *Planet. Space Sci.* **35**, 61 (1987).
- ¹⁴H. Laakso, *J. Atmos. Sol.-Terr. Phys.* **64**, 1735 (2002).
- ¹⁵Y. Miyake and H. Usui, *Phys. Plasmas* **16**, 062904 (2009).
- ¹⁶Solar Probe Plus: Report of the Science and Technology Definition Team, NASA Technical Memorandum 214161, July (2008).
- ¹⁷“Solar Orbiter assessment study report” (SRE-2009-5), European Space Agency, 2009.
- ¹⁸R. P. Lin, K. A. Anderson, S. Ashford, C. Carlson, D. Curtis, R. Ergun, D. Larson, J. McFadden, M. McCarthy, G. K. Parks, H. Rème, J. M. Bosqued, J. Coutelier, F. Cotin, C. D’uston, K.-P. Wenzel, T. R. Sanderson, J. Henrion, J. C. Ronnet, and G. Paschmann, *Space Sci. Rev.* **71**, 125 (1995).
- ¹⁹J. G. Laframboise and J. Luo, *J. Geophys. Res.* **94**, 9033, doi:10.1029/JA094iA07p09033 (1989).
- ²⁰E. G. Mullen, M. S. Gussenhoven, D. A. Hardy, T. A. Aggson, B. G. Ledley, and E. Whipple, *J. Geophys. Res.* **91**, 1474, doi:10.1029/JA091iA02p01474 (1986).
- ²¹I. Katz, M. Mandell, G. Jongeward, and M. S. Gussenhoven, *J. Geophys. Res.* **91**, 13,739, doi:10.1029/JA091iA01p00013 (1986).
- ²²J. G. Laframboise and L. J. Sonmor, *J. Geophys. Res.* **98**, 337, doi:10.1029/92JA00839 (1993).
- ²³S. T. Lai, *J. Geophys. Res.* **96**, 19,269, doi:10.1029/91JA01653 (1991).
- ²⁴R. L. Guernsey and J. H. M. Fu, *J. Geophys. Res.* **75**, 3193, doi:10.1029/JA075i016p03193 (1970).
- ²⁵J.-F. Roussel and J.-J. Berthelier, *J. Geophys. Res.* **109**, A01104, doi:10.1029/2003JA009836 (2004).
- ²⁶C. M. Cully, R. E. Ergun, and A. I. Eriksson, *J. Geophys. Res.* **112**, A09211, doi:10.1029/2007JA012269 (2007).